Transport Phenomena and Droplet Formation During Pulsed Laser Interaction With Thin Films

D. A. Willis

X. Xu[1]
e-mail: xxu@ecn.purdue.edu

School of Mechanical Engineering,
Purdue University,
West Lafayette, IN 47907

This work investigates transport phenomena and mechanisms of droplet formation during a pulsed laser interaction with thin films. The surface of the target material is altered through material flow in the molten phase induced by a tightly focused laser energy flux. Such a process is useful for developing a laser-based micromachining technique. Experimental and numerical investigations of the laser-induced fluid flow and topography variations are carried out for a better understanding of the physical phenomena involved in the process. As with many machining techniques, debris is often generated during laser-material interaction. Experimental parametric studies are carried out to correlate the laser parameters with the topography and droplet formations. It is found that a narrow range of operation parameters and target conditions exists for "clean" structures to be fabricated. The stop action photography technique is employed to capture the surface topography variation and the melting development with a nanosecond time resolution and a micrometer spatial resolution. Numerical simulations of the laser-induced surface deformation are also performed to obtain the transient field variables and to track the deforming surface. The comparison between the numerical and experimental work shows that, within the energy intensity range investigated in this work, the surface deformation and droplet formation are attributed to the surface-tension-driven flow, and the recoil pressure effect plays an insignificant role in the surface topography development. [S0022-1481(00)02903-0]

Keywords: Heat Transfer, Instability, Laser, Surface Tension, Visualization

1 Introduction

Droplet formation is a common problem in laser machining. Many studies have attributed droplet formation to fluid flow instabilities that develop from disturbances in the molten surface of the target ([1]). These disturbances lead to a wavy surface due to thermocapillary effects, which grow into surface structures due to the capillary wave instability. Droplets may then form from the capillary wave instability itself, or due to other instability mechanisms. The initial temperature disturbances can be attributed to a number of factors, including laser spatial intensity distributions that oscillate over time, as is the case with non-Gaussian laser beams, or a surface roughness that may cause nonuniform absorption of the incident laser beam.

The purpose of this work is to study the transport phenomena and droplet formation in a pulsed laser thin film interaction. Little work has been done on analyzing droplet formation arising from the use of lasers with Gaussian intensity distribution where the fluid flow is dominated in the radial direction. Because of the intensity distribution of the Gaussian laser beams, it is doubtful that capillary wave instabilities are contributing factors to droplet formation. Balandin et al. [2] studied the flow of iron containing surface active impurities irradiated by a nanosecond pulsed laser. No discussion of droplet formation was included. Dimitrov [3] observed droplets in his study but gave no explanations or theories to the droplet mechanisms either. Bennett et al. [4] used a finite element method to study the fluid flow and heat transfer in a nanosecond pulsed laser texturing process of magnetic disk substrates. Fluid flow was attributed to both thermocapillary and chemicapillary forces. The chemicapillary forces resulted from mass diffusion of phosphorous due to a concentration gradient

caused by depletion of phosphorous at the free surface. Willis et al. [5] performed a parametric study which demonstrated that for a narrow range of laser pulse energy, holes could be formed due to the flow in the radial direction as shown in Fig. 1, with no debris found in the surrounding area. However, above this narrow energy range, the strong radial flow could lead to droplet formation.

In a pulsed laser micromachining process, flow acceleration is high. Common instability mechanisms such as Rayleigh-Taylor or Kelvin-Helmholtz can occur. The Rayleigh-Taylor instability occurs when two superposed fluids of different densities are accelerated toward each other. If the density of the overlying fluid is less than the underlying fluid, the motion will be unstable for disturbance wavelengths greater than the critical wavelength, Λ_c, which is calculated by ([6]):

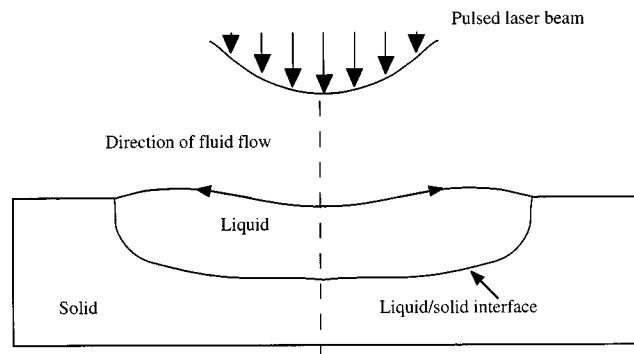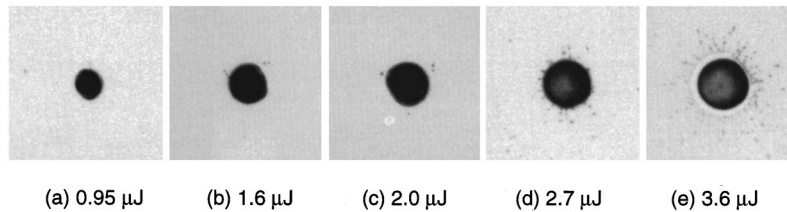$$\Lambda_c = 2\pi\left(\frac{\gamma}{g(\rho_1-\rho_2)}\right)^{1/2} \tag{1}$$

Fig. 1 Laser-induced phase change and Marangoni flow

(a) 0.95 μJ   (b) 1.6 μJ   (c) 2.0 μJ   (d) 2.7 μJ   (e) 3.6 μJ

Fig. 2 Results of experimental parametric study for 0.3 μm chromium film on quartz substrate

where ρ_1 is the density of the underlying fluid, ρ_2 is the density of the overlying fluid, γ is the surface tension, and g is the acceleration of gravity.

The Kelvin-Helmholtz instability can occur at the interface of two fluids of different density in relative horizontal motion. Flows will be stable for relative velocities given by the criteria

$$(v_1 - v_2)^2 < \frac{2(\rho_1 + \rho_2)\{\gamma g(\rho_1 - \rho_2)\}^{1/2}}{\rho_1 \rho_2}. \qquad (2)$$

The critical wavelength above which instability can develop for the Kelvin-Helmholtz instability is also given by Eq. (1). It should be noted that Eqs. (1)–(2) are approximations developed for inviscid, two-dimensional flows. In reality, flow instabilities will be three dimensional in nature, possibly due to nonuniform heating by the laser, which will lead to nonuniform velocity, density, and recoil pressure distributions.

In the pulsed laser-induced fluid flow, the gravitational force is small compared to the acceleration forces that result from the large surface tension gradient at the molten surface. The gravitational term in the above equations therefore should be replaced with a flow acceleration term in a flow stability analysis.

In this work, the possible mechanisms of droplet formation during pulsed laser interaction with thin chromium films are investigated. An in situ photography technique with a nanosecond time resolution is employed. This experiment shows the transient topography changes of a thin chromium film irradiated by a pulsed Nd:YLF laser with a 20-nsec pulse width. A numerical code is used to calculate the transient velocity and temperature fields and free surface motion. Results of experimental and numerical work are used to analyze the possible mechanisms of droplet formation.

2 Experimental Study

A parametric study ([5]) was performed on laser machining of thin chromium films deposited on glass substrates. Topography changes and debris formation patterns induced by a pulsed Nd:YLF laser were investigated. A narrow range of energy density levels was found in which debris-free surface structures could be obtained. This energy range lies between a threshold for hole formation at low energy, and a threshold for droplet formation. At low pulse energy, above the threshold for hole formation, the pulse energy is large enough that surface-tension gradients induce hole opening. As pulse energy increases, radial flow becomes rapid enough that inertial effects dominate and cause droplets to separate from the molten pool. A summary of the resulting topography changes and droplet formations resulting from 20-nsec pulses focused to a 9.5-μm radius is shown in the microphotographs in Fig. 2. A debris-free 7.5-μm diameter hole created in the chromium film by a 0.95-μJ pulse is shown in Fig. 2(a). Increasing pulse energy to 1.6 μJ resulted in a 10-μm hole diameter and formation of droplets. At this energy level the holes are still relatively clean since few droplets are formed; however, increasing the energy further increases the number of droplets. This is seen in Fig. 2(c) for an 11-μm hole created by a 2.0-μJ laser pulse. Figure 2(d) again shows an increased number of droplets for a 13-μm hole resulting from a 2.7-μJ pulse. This pattern continues as energy increases, and the droplets become uniformly

dispersed around the outer edge of the hole, as seen in Fig. 2(e) for a 15-μm hole created by a 3.6-μJ pulse. Atomic Force Microscopy verified that the surface deformations seen in Fig. 2 are holes. The holes created by 0.9 and 2.1-μJ pulses are shown in Fig. 3. The 0.9-μJ pulse energy is just above the threshold for hole formation, and the resulting hole is asymmetric. However, the hole does show that material is displaced to the outer edge of the hole and built up around the edges due to the surface-tension-driven flow as illustrated in Fig. 1. The 2.1-μJ pulse energy shows a similar pattern with improved symmetry. Power densities in this study are on the order of 62 MW/cm² for the highest energy used. No plasma is formed at the highest laser power density.

An in situ photography technique, the stop action photography, is developed to capture the transient melting and fluid flow processes ([5]). The experimental diagram is shown in Fig. 4. A pulsed nitrogen laser pumped dye laser with a visible wavelength of 600 nm and pulse width of 2.5 nsec was used to illuminate the surface of the specimen. The dye laser illuminates the specimen through a long working distance microscope objective system, which magnifies the specimen surface by 400x. Both the dye laser and the Nd:YLF laser are triggered by a pulse-delay generator. The delay between the two laser pulses is controlled by the pulse-delay generator, such that the dye laser is triggered after the Nd:YLF laser and exposes the film at the desired time. A 35-mm camera captures the illumination of the dye laser and stops the motion of the fluid on film. A 600-nm filter with a 40-nm bandwidth is placed in front of the camera to remove any light from sources other that the nitrogen laser pumped dye laser. This elimi-
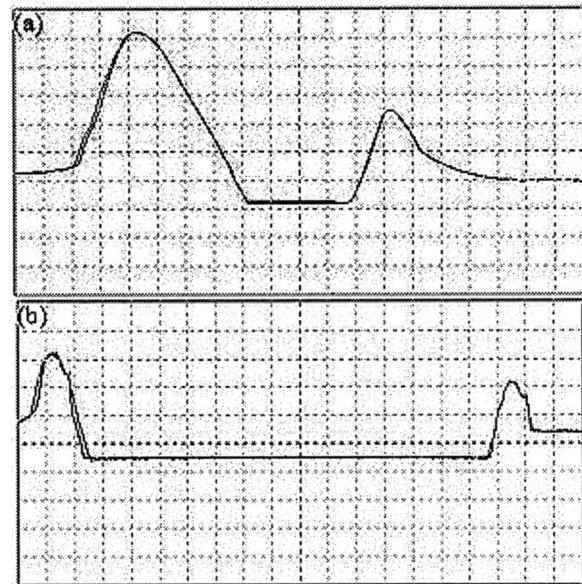
Fig. 3 AFM results: (a) 0.9 μJ pulse. Vertical scale is 0.4 μm/div., horizontal scale is 0.86 μm/div. (b) 2.1 μJ pulse. Vertical scale is 0.3 μm/div., horizontal scale is 1.1 μm/div.
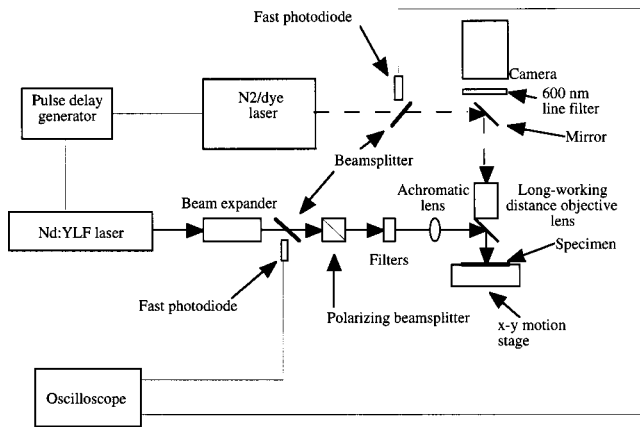
Fig. 4 Experimental diagram of stop-action photography

Fig. 5 Transient micrographs of 0.3-μm chromium film irradiated by 2.0-μJ 20-nsec laser pulses. Indicated time is with respect to the beginning of the laser pulse at $t=0$.

nates infrared light from the Nd:YLF laser that is reflected from the specimen surface, and thermal emission from the specimen surface and hot vapor. Only one photograph can be taken of each hole resulting from a laser pulse, therefore many photographs were taken at each pulse energy level and trigger delay setting. The experiments were repeatable, and the photos shown are representative of the results of several experiments at each delay time. The actual delay is measured by two fast photodiodes, and corrections are made for differences in optical path lengths and times for signals to reach the oscilloscope through cables. The measured delay is between laser peaks by approximating temporal distributions of the lasers as triangles. Two photographs are taken of each hole, one in situ, and the other several seconds after the laser pulse has ended (∞). Comparison of the two photographs allows the determination of the time at which changes in the hole geometry have ended. The 35-mm camera views an area of approximately 250×250 μm, which limits the resolution of the optical system since only a small area of approximately 60 $\times60$ μm is of interest in experiment. Only enlargements of the area of interest are presented.

The stop action photography is performed for 20-nsec full-width half-maximum (FWHM) laser pulses incident on 0.3-μm chromium films deposited by DC sputtering in ultrahigh vacuum. The focused laser radius is again 9.5 μm. The parametric study (Fig. 2) showed that randomly dispersed droplets were created around the outer edge of the hole for the 1.6, 2.0, and 2.7-μJ pulses, with the number of droplets increasing with pulse energy. The 3.6-μJ pulse increased the number of droplets and scattered them further away from the edge of the hole as seen in Fig. 2(e). The in situ photographs for a 2.0-μJ experiment are shown in Fig. 5. Surface deformation within the laser-irradiated zone is seen at 11 nsec. The deformed region within the laser-irradiated zone undergoes a rapid change between 17 and 34 nsec as shown in Figs. 5($b-d$). There is also a central region which has a higher reflectivity than the rest of the deformed area, Figs. 5($d-j$). This central region decreases in brightness with time until it is not visible in the 150-nsec photo in Fig. 5(k). The explanation for the high reflectivity spot is that the surface tension gradient is lower near the center of the laser-irradiated zone than it is near the outer edge of the laser-irradiated zone. Therefore, the center area of the irradiated zone does not begin to flow as early as the outer region. As time progresses, the flow pulls the chromium away from the center of the molten pool, leaving only glass in the center and thus decreasing the reflectivity. After 249 nsec no changes are seen in the surface geometry, indicating that the surface deformation process is complete. The final hole diameter is approximately 11 μm. Note that the photographs taken by the stop action photography (Fig. 5) have slightly poorer spatial resolution than those taken
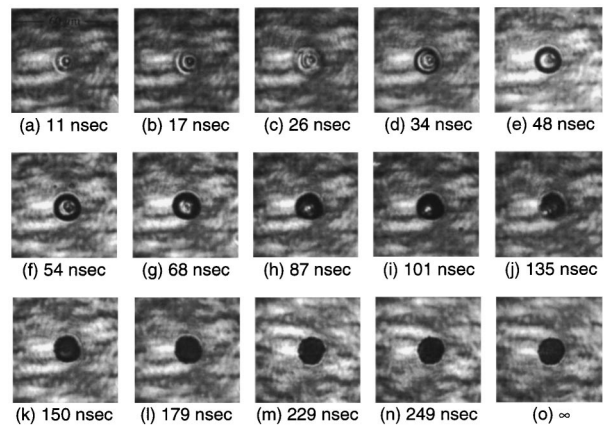
under an optical microscope after the process is complete (Fig. 2). Individual droplets are not clearly seen in Fig. 5.

Photographs of the transient surface topography resulting from 2.7-μJ laser pulses are shown in Fig. 6. Surface deformation is visible at 14 nsec and the hole size increases little after this time. Similar to the 2.0-μJ experiment, a central high reflectivity spot appears within the laser-irradiated zone that dissipates in brightness with time. The modified area becomes distorted at the outer edge between 98 and 184 nsec. This is the unstable fluid flow leading to the formation and separation of droplets. This distortion is due to scattering of light by droplets in all directions, making less light incident on and reflected off the target. This results in a blurring effect, making the holes appear larger, thus the final holes are smaller when compared to those in the intermediate times. Thermal lensing may also contribute to this blurring, but it only affects the very vicinity of the hole since the heat-affected zone, on the order of 1 micron, is much smaller than the blurred area. Individual droplets become visible in the photograph at 184 nsec. After 283 nsec no changes are seen in the hole diameter or droplet patterns surrounding the hole, indicating that the surface modification process is complete. The final hole diameter is approximately 13 μm.

Photographs of the transient surface topography induced by 3.6-μJ laser pulses are shown in Fig. 7. Surface deformation is seen at 14 nsec followed by expansion of the deformed area until 25 nsec. A central high reflectivity spot, similar to those seen in
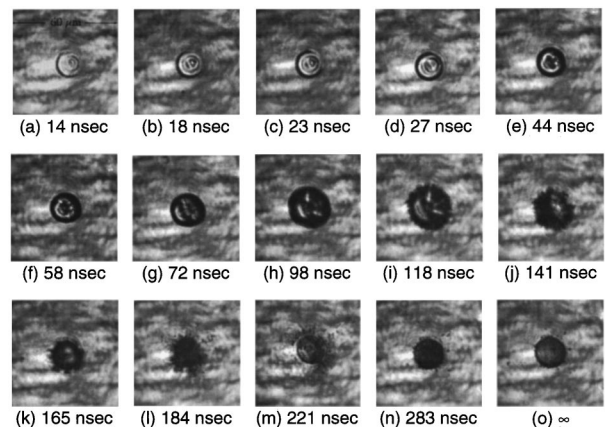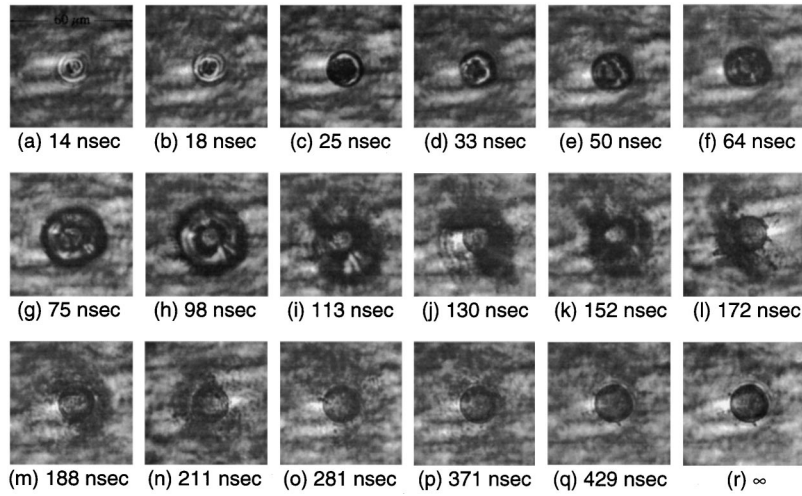

Fig. 6 Transient micrographs of 0.3-μm chromium film irradiated by 2.7-μJ 20-nsec laser pulses. Indicated time is with respect to the beginning of the laser pulse at $t=0$.

Fig. 7 Transient micrographs of 0.3-μm chromium film irradiated by 3.6-μJ 20-nsec laser pulse. Indicated time is with respect to the beginning of the laser pulse at $t=0$.

Figs. 5–6, is also seen in the photographs at 3.6 μJ, but this bright spot diminishes after 50 nsec. Similar to the previous experiments, the outer edge becomes distorted from 64 to 152 nsec due to the separation of droplets from the edge of the hole. Changes in the surface topography continue much longer in this experiment, and droplets are not seen until 281 nsec, as seen in Fig. 7(o). The flow has ceased at 429 nsec since no changes in the surface topography are seen after this time. The final hole diameter is approximately 15 μm.

The three in situ experiments presented here all indicate melting within the first 20 nsec of the laser pulse, with rapid hole expansion while the laser pulse is incident on the surface. Fluid flow is observed long after the laser pulse is completed at 40 nsec and lasts for over 250 nsec. Solidification time increases with increasing pulse energy, ranging from approximately 249 nsec for a 2.0-μJ pulse, to about 429 nsec for a 3.6-μJ pulse. The experiments show rapid flow development and droplet formation *after* the end of the laser pulse. The flow lasts longer with increasing pulse energy.

3 Numerical Modeling

A numerical model of the pulsed laser surface modification process is developed. The energy transfer and fluid flow induced by the laser irradiation are governed by the mass, momentum, and energy conservation equations

$$\nabla \cdot \mathbf{v}=0 \tag{3}$$

$$\rho \frac{\partial \mathbf{v}}{\partial t}+\rho(\mathbf{v}\cdot\nabla)\mathbf{v}=-\nabla p+\nabla(\mu\nabla\cdot\mathbf{v}) \tag{4}$$

$$\rho \frac{\partial h}{\partial t}+\rho(\mathbf{v}\cdot\nabla h)=\nabla\cdot\left(\frac{k}{c_p}\nabla h\right)+Q \tag{5}$$

In these equations, $\mathbf{v}$ is the velocity vector, p the pressure, and h the enthalpy. The thermophysical properties ρ, μ, k, and c_p are, respectively, the density, viscosity, thermal conductivity, and specific heat. The enthalpy method ([7]) is employed in the energy equation, Eq. (5), to calculate the solid-liquid phase change. Phase transition in the glass substrate is neglected, and flow of the softened glass is neglected due to its high viscosity. The volumetric heating term Q is used to describe the nonuniform absorption of the laser energy in the target, since the laser energy is absorbed exponentially along the optical axis, and is Gaussian in distribution along the radius of the laser beam. The absorption of laser energy is modeled as instantaneous heating with a triangular tem-

poral distribution of 20 nsec (FWHM). Therefore, the entire length of the laser pulse is 40 nsec. The absorbed laser energy is estimated by calculating the reflectivity of chromium at the laser wavelength, which is calculated from the complex index of refraction of chromium to be 63 percent.

At the surface of the laser melted region, fluid flow is induced due to the tangential forces of the surface tension gradient created by the temperature gradient along the free surface. Therefore, the boundary condition at the free surface in the tangential direction is expressed as

$$\mathbf{t}\cdot\tau=\mathbf{t}\cdot\nabla\gamma+(\mathbf{t}\cdot\nabla T)\frac{\partial\gamma}{\partial T}=\mu\mathbf{n}\cdot\nabla(\mathbf{v}\cdot\mathbf{t}) \tag{6}$$

The boundary condition normal to the free surface is the balance between the normal component of the surface traction vector and the surface tension forces due to the curved free surface and the pressure

$$\mathbf{n}\cdot\tau=-\frac{\gamma}{R_c}-p_r \tag{7}$$

where R_c is the radius of curvature, p_r is the recoil pressure, and γ is the surface tension. The equation that governs variations of the free surface with time is given by

$$\frac{\partial\Sigma}{\partial t}+\mathbf{v}\cdot\nabla\Sigma=0 \tag{8}$$

where Σ is the free surface geometry.

At the free surface, the recoil pressure is related to surface temperature by the kinetic theory ([8]) as

$$p_r=p_o\exp\left\{\frac{\Delta H_{lv}(T-T_{lv})}{RTT_{lv}}\right\} \tag{9}$$

The molar mass flux, $\bar{j}_v$ due to evaporating atoms at the free surface is given by ([8])

$$\bar{j}_v=Ap_r(2\pi MRT)^{-1/2} \tag{10}$$

and this molar mass flux is related to the thermal boundary condition at the evaporating surface as

$$k_l\nabla T=-\Delta H_{lv}\bar{j}_v. \tag{11}$$

Equations (9)–(11) are used as boundary conditions for the energy equation. p_o is the atmospheric pressure, ΔH_{lv} is the enthalpy of vaporization, T_{lv} is the equilibrium boiling temperature, T is the

Table 1   Thermophysical properties of chromium ([10,18–22])

Melt Temperature	2133 K	Enthalpy of Fusion	16.933 kJ/mol
Equilibrium Boiling Temperature	2953 K	Enthalpy of Vaporization	344.3
Refractive Index @ $\lambda = 1.047\ \mu$m	$4.52 + i4.29$	Molar Weight	52.01 kg/kmol
Activation Energy	$E = 55$ kJ/mol	Density	7100 kg/m^3
Viscosity at Melt Temperature	$\mu = 0.000684$ kg/m·sec		
Surface tension	$\gamma = 1.700 - 0.00032(T - T_m)$ N/m		
Thermal Conductivity	$k = 69.9 + 0.15979T - 0.0004212T^2 + 3.9265 \times 10^{-7}T^3$ $- 1.5974 \times 10^{-10}T^4 + 2.4025 \times 10^{-14}T^5$ W/m·K		
Specific Heat	$c_p = 236.23 + 1.0788T - 0.0015052T^2 + 9.7379 \times 10^{-7}T^3$ $- 1.8628 \times 10^{-10}T^4$ J/kg·K		

surface temperature, and R is the universal gas constant. In Eq. (10), A is a ''sticking coefficient,'' which is the fraction of vapor particles hitting the surface that stick to it. For metals, the value of A is approximately unity ([8]).

Boundary conditions at the far field are given by

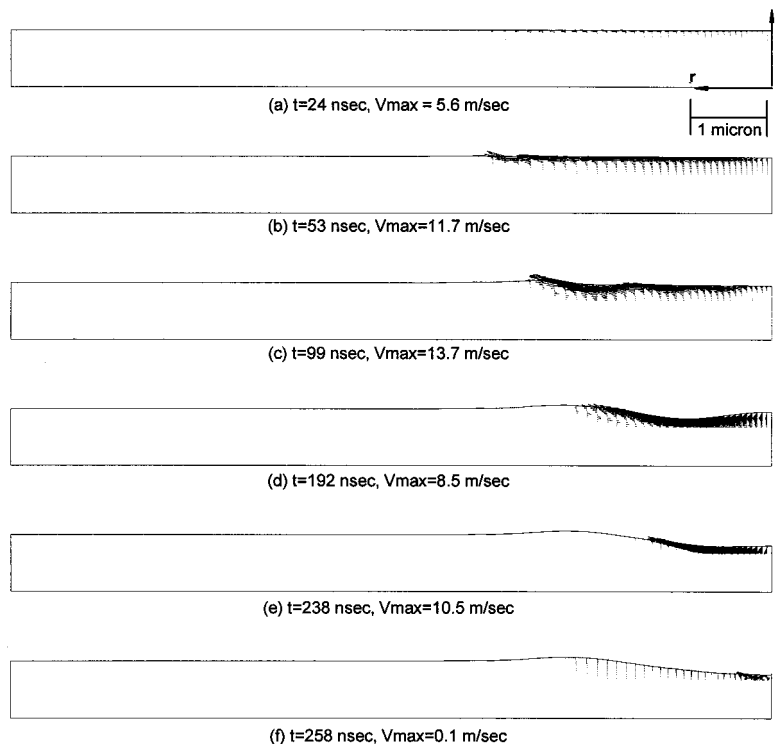$$\mathbf{v} = 0 \tag{12}$$

$$\nabla T = 0. \tag{13}$$

A no-slip boundary condition is used at the chromium/glass interface, because the dynamics of three-phase interface is not well known and thus not considered in this work. Numerical calculations are carried out using the computational fluid dynamics code, FIDAP (Fluent Inc., Lebanon, NH). The system is modeled as two-dimensional axisymmetric due to the symmetry of the incident laser beam. Thermophysical properties used in the simulations are listed in Table 1. Whenever possible, temperature-dependent material properties are used. The temperature dependence of viscosity is modeled as an Arrhenius relationship given by ([9,10])
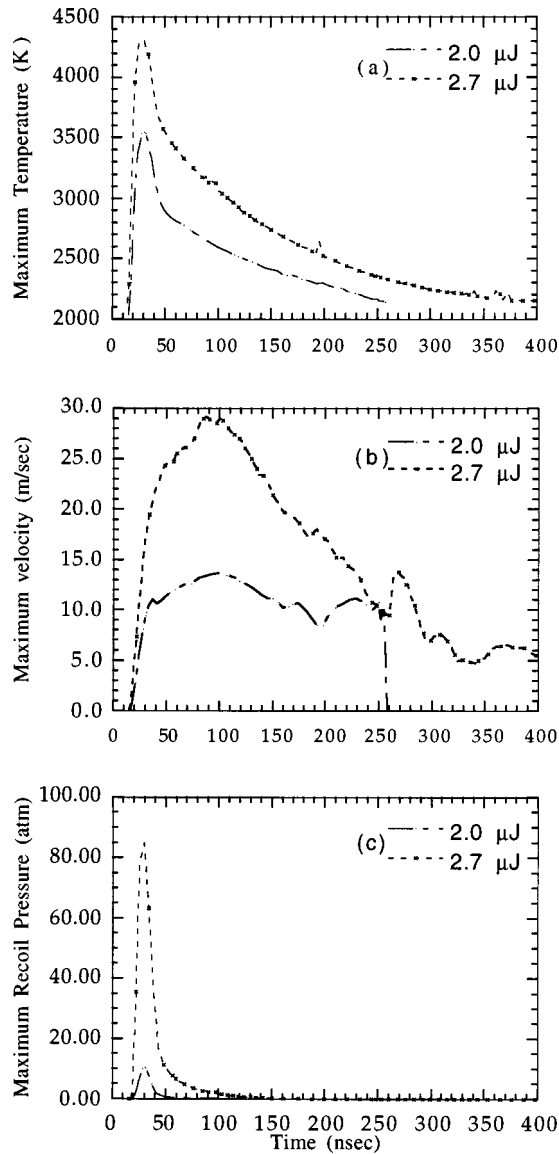
$$\mu = \mu_o \exp(E/RT) \tag{14}$$

where μ_o is a reference viscosity which is normalized such that Eq. (14) results in the viscosity at the melting temperature given in Table 1 when the melting temperature is used in Eq. (14). E is the activation energy and is estimated by ([9])

$$E = 0.431T_m^{1.348} \tag{15}$$

The surface tension data are for pure chromium obtained from Brandes and Brook [10]. The original values are from Allen ([11,12]) which were measured at the melting temperature ([11]) and calculated for higher temperatures ([12]). The surface tension of metals that have been exposed to atmospheric conditions will have chemically active surface impurities such as oxygen and sulfur. It has been reported that these surface active impurities will alter the surface tension significantly, such that the surface tension can actually increase at temperatures slightly above the melting temperature ([13–15]). Bostanjoglo and Nink [16] and Balandin et al. [2] reported that the effect of an increased surface tension above the melting point in metals during laser melting of thin films could cause thickening of the thin film at the center of the laser spot. Therefore, the effect of oxidation could be significant.

(a) t=24 nsec, Vmax = 5.6 m/sec

1 micron

(b) t=53 nsec, Vmax=11.7 m/sec

(c) t=99 nsec, Vmax=13.7 m/sec

(d) t=192 nsec, Vmax=8.5 m/sec

(e) t=238 nsec, Vmax=10.5 m/sec

(f) t=258 nsec, Vmax=0.1 m/sec
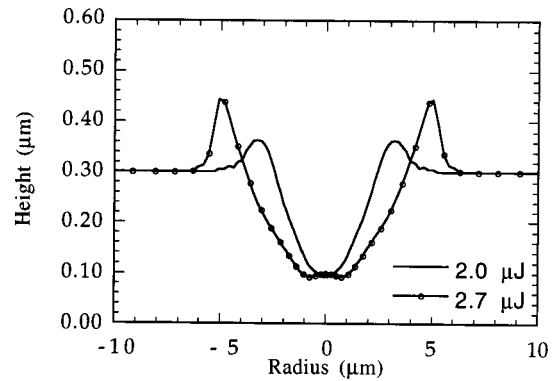
Fig. 8   Calculated transient velocity field of a 0.3-μm chromium film irradiated by a 2.0-μJ, 20-nsec laser pulse

Fig. 9 Transient (*a*) center node temperature, (*b*) maximum velocity, and (*c*) center node recoil pressure of 0.3-μm chromium film irradiated by 2.0 and 2.7-μJ 20-nsec pulses

Fig. 10 Final surface topography of 0.3-μm chromium film irradiated by 2.0 and 2.7-μJ 20-nsec incident laser pulses

However, for chromium with oxygen and sulfur impurities, the only experimental data in literature shows a negative temperature coefficient ([17]). Therefore, only a negative temperature coefficient of surface tension is considered in the simulation.

Calculations are performed for incident laser pulse energies of 2.0 and 2.7 μJ with 20 nsec pulse width (FWHM) and a radius of 9.5 μm incident on a 0.3 μm chromium film. A domain with a radius of 12 μm and axial depth of 0.9 μm is used. The axial depth consists of the 0.3-μm thin chromium film and a 0.6-μm glass substrate. The glass substrate is much thinner than that used in the experiments; however, the thermal penetration depth into the glass is very small within the time period of interest, approximately 0.13 μm. Due to the same reason, the domain size in the radial direction, 12 μm, is large enough to contain the temperature and fluid field development. The grid size of the thin film is 60 nodes in the radial direction and 12 nodes in the axial direction. A grid independence study is performed for the 2.0 μJ, 20 nsec laser pulse by varying the number of grids in the radial direction. Grid sizes of 60×12 and 80×12 were tested and little differences were found. The Quasi-Newton (Broyden's update) method is used to

solve the system of nonlinear equations. Time integration is performed by the backward Euler method. Approximately 200 hours of CPU time is required to complete each simulation on a Hewlett Packard 715/50.

The transient velocity field resulting from a 2.0 μJ pulse is plotted as a half-domain in Fig. 8, with the *z*-axis as the axis of symmetry. The velocity field begins to develop on the thin melted surface layer halfway into the laser pulse, seen at 24 nsec in Fig. 8(*a*), and flows away from the center of the irradiated area due to the surface tension gradient along the free surface. The flow accelerates to 11.7 m/sec at a time of 53 nsec in Fig. 8(*b*), and the velocity peaks at 13.7 m/sec at 99 nsec, and decreases slowly after this time. The velocity is still well developed with a maximum velocity of 8.5 m/sec at a time of 192 nsec, as seen in Fig. 8(*d*). At 238 nsec, the maximum velocity has actually increased when the location of the maximum velocity is moving toward the center of the irradiated zone. The size of the velocity field has decreased significantly since the molten pool is solidifying. The maximum velocity decreases rapidly until it is almost zero at 258 nsec, as seen in Fig. 8(*f*). Note that the fluid flow field does not develop until after the laser pulse has ended (40 nsec) and topography development occurs long after the laser pulse has ended. This can be seen in Figs. 8(*c–f*). These results compare well with the experimental results. The experimental study showed droplets outside of the holes, resulting from the high velocity radial flow away from the center of the molten pool. (This will also be discussed in Section 4.) The numerical results also correlate well with the in situ photography experiment, which showed flow development during the later half of the laser pulse, and rapid changes in the laser-irradiated area after completion of the laser pulse. The numerical model also shows that the center of the laser-irradiated zone will be thicker than the remaining modified area early in the process because the surface tension gradient is the lowest there, resulting in the lower velocity fluid flow.

The transient maximum temperature, velocity, and recoil pressure are plotted in Figs. 9(*a*), (*b*), and (*c*), respectively, for the 2.0 and 2.7-μJ laser pulses. The maximum temperature is reached at approximately 30 nsec, however, the fluid flow in the molten pool is still accelerating at this time for both laser energy levels. Figure 9(*b*) shows that the velocity continues to increase long after the end of the laser pulse. Note that the radial velocity in the molten pool increases rapidly when pulse energy increases, increasing inertial effects. Recoil pressure peaks at the same time as the maximum temperature (see Eq. (9)), and is only significant during the first 60 nsec of the process. Figure 8 shows that the topography of the free surface developed long after the laser pulse ended, therefore, it is unlikely that recoil pressure contributes significantly to the process. This is due to the fact that the topography development occurs long after the laser pulse has ended, while the recoil pressure is negligible after 50–60 nsec. In order to deter-

mine if recoil pressure has an impact on the results, simulations are performed with and without the recoil pressure term in Eq. (7) for both 2.0 and 2.7-μJ laser pulses. Due to the time required to perform a simulation with a temperature-dependent viscosity, the tests are performed using a constant viscosity. The results of the simulations show no changes in the transient velocity field or in the final surface topography. It is thus concluded that surface tension dominates the fluid flow, and that the recoil pressure has no significant influence on the processes studied in this work.

Plots of the final surface topography are shown in Fig. 10 for 2.0 and 2.7-μJ 20-nsec incident laser pulses. The 2.0-μJ pulse results in a hole that is approximately 8 μm in diameter and 0.2 μm deep. The 2.7-μJ pulse results in a hole that is approximately 12 μm in diameter and 0.2 μm deep. These diameters are smaller than the experimental values of approximately 11 μm for the 2.0-μJ pulse, and 13 μm for the 2.7-μJ pulse. The differences between the experimental and numerical hole sizes could be attributed to limitations of the numerical model. One of the limitations of the model is the limited knowledge of material properties. This is because thin film thermal properties and high-temperature thermal properties are not well known. The current model uses bulk material properties that are linearly extrapolated for high temperatures. Another limitation of the model is that the density change from the solid to liquid phase is not accounted for, which may affect the surface topography and the velocity field development.

4 Instability of the Laser-Induced Fluid Flow

The results of the experimental and numerical studies are used to analyze the instability mechanisms and droplet formation in the laser-induced molten pool. Although flow instabilities and droplet formation are not simulated due to their three-dimensional nature, the results of the two-dimensional model can be used to obtain acceleration data for an order of magnitude estimation. The calculations for the 2.0 and 2.7-μJ pulses predict maximum flow accelerations of approximately 3.53×10^8 m/sec^2 and 1.29×10^9 m/sec^2, respectively. Replacing the gravitational acceleration term in Eq. (1) with these acceleration values gives critical wavelengths of approximately 5.5 μm for the 2.0-μJ pulse and 2.9 μm for the 2.7-μJ pulse. These values are on the same order of magnitude as the molten pool diameter in the present study, therefore, perturbation in the molten pool can lead to a Rayleigh-Taylor instability development. Growth of such an instability could lead to a wavy surface, allowing droplets to initiate from the peaks of the waves. Inspection of Figs. 2(d–e) shows that the ridges of material around the holes have a wavy pattern, and Fig. 2(e) shows droplets connected to the peaks of the wavy ridge.

For the Kelvin-Helmholtz instability, if gravitational acceleration is used, Eq. (2) predicts flows to be stable for relative velocities less than 24 m/sec, which is on the same order of the calculated maximum velocity. However, the critical wavelength is on the order of 33 mm, much larger than the domain of interest in this study. On the other hand, if acceleration of the melt is used in Eqs. (1)–(2), the critical wavelength will decrease to the order of several microns; however, the relative velocity below which the flow is stable increases to values over 1000 m/s, much higher than the velocities encountered in the present study. Therefore, it is unlikely that the Kelvin-Helmholtz instability is present in the process.

The microphotographs of the laser-irradiated surface shown in Fig. 2 show droplets outside the edge of the holes. Numerical simulations and in situ photographs suggest that these droplets are due to the high radial flow velocity moving fluid away from the center of the molten pool after the laser pulse has ended. Droplets may form when the high velocity flow gains enough inertia to overcome the surface tension forces which hold the fluid together, allowing material to shear away from the ridge built up at the outer edge of the holes. The Weber number is a nondimensional ratio of inertial forces to surface tension forces and is defined as

$$\text{We} = \frac{\rho_1 v^2 L_c}{\gamma} \tag{16}$$

where v is the velocity, γ is the surface tension, and L_c is a characteristic length scale. Since resolutions of the current in situ experimental techniques are not good enough to measure the melt velocity, the calculated velocity values are used to estimate the Weber number. A value of 0.5 μm is used for the characteristic length, which is approximately the diameter of the droplets measured by SEM. For the 2.0-μJ simulation, a maximum velocity of 13.7 m/sec is achieved, and the Weber number is calculated to be approximately 0.34, which indicates that surface tension forces dominate. The Weber number for the 2.7-μJ simulation is calculated to be 1.56 at a maximum velocity of 29.1 m/sec, indicating that inertial forces dominate. These calculations of the Weber number correlate well with experiments, which show that a large increase of the number of droplets occurs when the laser pulse energy varies from 2 to 2.7 μJ.

5 Conclusions

Fluid flow and droplet formation occurring in a pulsed laser thin film interaction have been studied. Experimental in situ photography of the process shows rapid fluid flow after completion of the laser pulse with evidence of flow instability at the outer edges of the melted region. Results of a numerical model including the flow development and total time duration correlate well with experimental results. Instability analysis shows that the critical instability wavelength is smaller than the molten pool. Thus, perturbations in the molten pool larger than the critical wavelength may lead to instability development. The calculated Weber number also correlated well with droplet formation. It is concluded that the fluid flow and droplet formation are due to the surface-tension-driven flow, and the recoil pressure due to surface evaporation plays a minor role in the laser fluence range used in the work.

Nomenclature

A = sticking coefficient
c_p = specific heat
E = activation energy
G = gravitational acceleration
H = enthalpy
$\bar{j}_v$ = molar mass flux
k = thermal conductivity
L_c = characteristic length scale
M = molar weight
$\mathbf{N}$ = surface normal vector
P = pressure
P_r = recoil pressure
p_o = ambient pressure
Q = volumetric heat generation
R = universal gas constant
R_c = radius of curvature
$\mathbf{T}$ = surface tangential vector
T = temperature
T_{lv} = equilibrium boiling temperature
T_m = equilibrium melting temperature
$\mathbf{V}$ = velocity vector
V = velocity
We = Weber number

Greek Symbols

ΔH_{lv} = enthalpy of vaporization
Σ = free surface geometry
γ = surface tension
Λ_c = critical instability wavelength
ρ = density
τ = surface traction vector
μ = viscosity

Subscripts

1 = underlying fluid
2 = overlying fluid
l = liquid
s = solid

References

[1] Brailovsky, A. B., Gaponov, S. V., and Luchin, V. I., 1995, ''Mechanisms of Melt Droplets and Solid-Particle Ejection From a Target Surface by Pulsed Laser Action,'' Appl. Phys. A: Mater. Sci. Process., **61**, pp. 81–86.

[2] Balandin, V. Yu., Otte, D., and Bostanjoglo, O., 1995, ''Thermocapillary Flow Excited by Focused Nanosecond Laser Pulses in Contaminated Thin Liquid Iron Films,'' J. Appl. Phys., **78**, No. 3, pp. 2037–2044.

[3] Dimitrov, D. A., 1995, ''Some Observations on Laser Trimming Platinum Thin Films,'' Platinum Met. Rev., **39**, No. 3, pp. 129–132.

[4] Bennett, T. D., Krajnovich, D. J., Grigoropoulos, C. P., Baumgart, P., and Tam, A. C., 1997, ''Marangoni Mechanism in Pulsed Laser Texturing of Magnetic Disk Substrates,'' ASME J. Heat Transfer, **119**, pp. 589–596.

[5] Willis, D. A., Xu, X., Poon, C. C., and Tam, A. C., 1998, ''Laser-Assisted Surface Modification of Thin Chromium Films,'' Opt. Eng., **37**, No. 3, pp. 1033–1041.

[6] Chandrasekhar, S., 1961, *Hydrodynamic and Hydromagnetic Stability*, Oxford University Press, London.

[7] Shamsundar, N., and Sparrow, E. M., 1975, ''Analysis of Multidimensional Conduction Phase Change Via the Enthalpy Model,'' ASME J. Heat Transfer, **97**, pp. 333–340.

[8] von Allmen, M., 1987, *Laser-Beam Interactions With Materials* (Springer Series in Materials Science 2), Springer-Verlag, Berlin, pp. 146–151.

[9] Grosse, A. V., 1963, ''High Temperature Research,'' Science, **140**, pp. 781–789.

[10] Brandes, E. A., and Brook, G. B., 1992, *Smithells Metals Reference Book*, 7th Ed., Butterworth-Heinemann, Oxford.

[11] Allen, B. C., 1964, ''The Surface Tension of Liquid Chromium and Manganese,'' Trans. Metall. Soc. AIME, **230**, pp. 1357–1361.

[12] Allen, B. C., 1972, ''The Surface Tension of Liquid Metals,'' *Liquid Metals, Chemistry and Physics*, S. Z. Beer, ed., Marcel Dekker, New York, pp. 161–212.

[13] Vitol, E. N., and Orlova, K. B., 1984, ''The Surface Tension of Liquid Metals,'' Russ. Metall., **4**, pp. 34–40.

[14] Tret'yakova, E. E., Baum, B. A., Tyagunov, G. V., Klimenkov, E. A., and Tsepelev, V. S., 1986, ''Surface Tension of Molten Steel,'' Russ. Metall., **4**, pp. 25–28.

[15] Filippov, K. S., 1992, ''Density and Surface Tension of Iron and Fe-Cu-S Melts,'' Russ. Metall., **1**, pp. 46–48.

[16] Bostanjoglo, O., and Nink, T., 1997, ''Liquid Motion in Laser Pulsed Al, Co and Au Films,'' Appl. Surf. Sci., **109/110**, pp. 101–105.

[17] Chung, W. B., Nogi, K., Miller, W. A., and McLean, A., 1992, ''Surface Tension of Liquid Cr-O System,'' Mater. Trans., JIM, **33**, No. 8, pp. 753–757.

[18] Martynyuk, M. M., 1983, ''Critical Constants of Metals,'' Russ. J. Phys. Chem., **57**, No. 4, pp. 494–501.

[19] Barin, I., 1993, *Thermochemical Data of Pure Substances, Part I, Ag–Kr*, VCH, Weinheim, Germany, pp. 418–419.

[20] Incropera, F. P., and DeWitt, D. P., 1990, *Fundamentals of Heat and Mass Transfer*, 3rd Ed., John Wiley and Sons, New York, p. A3.

[21] Hunter, W. R., and Lynch, D., 1991, ''An Introduction to the Data for Several Metals,'' *Handbook of the Optical Constants of Solids II*, E. D. Palik, ed., Harcourt Brace Jovanovich, Boston, Part II, Subpart I, pp. 374–385.

[22] Boyer, H. E., and Gall, T. L., 1983, *Metals Handbook Desk Edition*, American Society for Metals, Metals Park, OH, p. 2.19.